

Voltage-controlled tunneling magnetoresistance in all-antiferromagnetic tunnel junctions based on noncollinear antiferromagnet Mn3Sn

Ying Su(苏颖), Tian Zhao(赵甜), Fei Xu(许飞), Bohao Ye(叶博豪), Hongting He(何泓霆), Yan Liu(刘艳), Qin Wang(王钦), Shengbo Sang(桑胜波), Yang Ge(葛阳)

Citation: Chin. Phys. B. 35, 097504 (2026). DOI: 10.1088/1674-1056/ae9267 | CSTR: 32038.14.CPB.ae9267
http://cpb.iphy.ac.cn; http://iopscience.iop.org/cpb

What follows is a list of articles you may be interested in

First-principles investigation of magnetic properties in hyperkagome Mn3TSi (T = Co, Rh, Ir) lattice

Peng Ren(任鹏), Xiaosheng Ni(倪晓升), Xunwu Hu(胡训武), Kun Cao(曹坤)

Chin. Phys. B. 35, 057502 (2026). DOI: 10.1088/1674-1056/ae156c | CSTR: 32038.14.CPB.ae156c

Magnon polarons: Hybrid quasiparticles in coupled spin–lattice systems

Yufei Li(李宇飞), Qi Gu(古琪), Mingzhi Wang(王铭志), Jia-Min Lai(来嘉敏), Aizhuo Zhang(张爱茁), Yameng Guo(郭雅萌), Yuhao Xia(夏宇浩), Yaowen Liu(刘要稳), Jianwei Zhang(张建卫), Wei Zhang(张伟), Zhiyong Quan(全志勇), Zhong Shi(时钟), Xiaohong Xu(许小红)

Chin. Phys. B. 35, 047507 (2026). DOI: 10.1088/1674-1056/ae5efc | CSTR: 32038.14.CPB.ae5efc

Efficient magnon transport and magnon torque through the epitaxial antiferromagnetic insulator α-Fe2O3

Donglin Song(宋东霖), Fanyu Meng(孟凡毓), Mingyang Sun(孙铭扬), Hongrui Ni(倪泓睿), Jinhao Zou(邹锦豪), Zichen Yao(姚子忱), Zhenlong Guo(郭振龙), Yichi Zhang(张一驰), Liyan Zhang(张丽艳), Hongliang Bai(白洪亮), Wenping Zhou(周文平), Yi Wang(王译)

Chin. Phys. B. 35, 047505 (2026). DOI: 10.1088/1674-1056/ae48c1 | CSTR: 32038.14.CPB.ae48c1

Strong magnon–photon coupling in on-chip CoFe/LiNbO3 hybrid nanostructures

Jinlong Wang(王锦龙), Rundong Yuan(袁润东), Manuel Mueller, Luis Flacke, Hanchen Wang(王涵晨), Kanglin Yu(俞康麟), Junfeng Hu(胡俊峰), Fenglin Zhong(钟丰麟), Jilei Chen(陈济雷), Mathias Weiler, Matthias Althammer, Haiming Yu(于海明)

Chin. Phys. B. 35, 047503 (2026). DOI: 10.1088/1674-1056/ae2d3c | CSTR: 32038.14.CPB.ae2d3c

Non-Markovian dynamical solver for efficient combinatorial optimization

Haijie Xu(徐海杰), Zhe Yuan(袁喆)

Chin. Phys. B. 35, 027503 (2026). DOI: 10.1088/1674-1056/ae1fea | CSTR: 32038.14.CPB.ae1fea

---

Voltage-controlled tunneling magnetoresistance in all-antiferromagnetic tunnel junctions based on noncollinear antiferromagnet Mn_3Sn

Ying Su(苏颖)[1,2], Tian Zhao(赵甜)[1,2], Fei Xu(许飞)[1,2], Bohao Ye(叶博豪)[1,2], Hongting He(何泓霆)[1,2], Yan Liu(刘艳)[1,2], Qin Wang(王钦)[4], Shengbo Sang(桑胜波)[1,2], and Yang Ge(葛阳)[1,2,3,†]

[1] *Shanxi Key Laboratory of Micro Nano Sensors & Artificial Intelligence Perception, College of Integrated Circuits, Taiyuan University of Technology, Taiyuan* 030024, *China*

[2] *Key Laboratory of Advanced Transducers and Intelligent Control System of the Ministry of Education, Taiyuan University of Technology, Taiyuan* 030024, *China*

[3] *Shanxi Research Institute of 6D Artificial Intelligence Biomedical Science, Taiyuan* 030024, *China*

[4] *Institute of Energy Innovation (IEI), College of Materials Science and Engineering, Taiyuan University of Technology, Taiyuan* 030024, *China*

(Received 15 April 2026; revised manuscript received 11 July 2026; accepted manuscript online 30 July 2026)

Unlike traditional antiferromagnetic materials (AFMs), kagome-based non-collinear antiferromagnets (NCAFs) (Mn_3X, X = Sn, Ge, Ga, etc.) exhibit a local spin-splitting effect and ultrafast dynamics, which are expected to enable the construction of all-antiferromagnetic tunnel junctions (AATJs) with negligible stray fields. Herein, we revealed the non-collinear magnetization switching mechanisms of Mn_3Sn and constructed the AATJs models with Mn_3Sn as free layer and reference layer by employing the non-equilibrium Green's function combined with density-functional theory. We achieved tunnelling magnetoresistance (TMR) ratios of approximately 131% at room temperature in Mn_3Sn/MgO/Mn_3Sn structure by manipulation of their Néel vectors. Particularly, we explored the dependence of TMR on bias voltages in non-equilibrium states, and the results show the TMR ratio can be regulated from 42% to 20% by applied bias. Our work presents the great potential of developing MRAM with ultra-high-speed, low-power consumption and high-density integration based on non-collinear antiferromagnets as the core functional units.

Keywords: non-collinear antiferromagnets, Néel vectors, tunneling magnetoresistance, tunnel junction, transmission coefficients

PACS: 75.50.Ee, 75.47.–m, 73.40.Gk

DOI: 10.1088/1674-1056/ae9267 **CSTR:** 32038.14.CPB.ae9267

1. Introduction

Magnetic tunnel junctions (MTJs) based on TMR effects have much higher magnetic field sensitivity,[1,2] higher tunneling magnetoresistance ratio, and faster read speed, which have been considered as the key components in magnetic random access memory (MRAM).[3,4] To date, the majority of MTJs composed of ferromagnetic materials are easily disturbed by an external magnetic field due to a certain finite magnetization. In the meanwhile, there still exists a long turnover time of magnetic moment and high turnover current density,[5] which is unable to meet the ultra-high-speed, low-power, and high-stability development requirements of the novel/next-generation MRAM.

Antiferromagnetic materials (AFMs) feature zero stray field,[6] ultrafast magnetic response, and strong immunity to magnetic perturbations.[7,8] Traditionally, AFMs have been used as exchange-bias reference layers in ferromagnetic MTJs.[9] Recently, kagome-structured non-collinear antiferromagnets (NCAFs) have attracted intensive interest due to their local spin-splitting, negligible stray field, and ultrafast switching behavior.[10,11] Typical NCAFs include hexagonal Mn_3X (X = Sn, Ge, Ga) and cubic Mn_3X (X = Pt, Ir). Notably, Mn_3Sn exhibits nonzero Berry curvature via time-reversal symmetry (TRS) breaking,[12] leading to a pronounced anomalous Hall effect.[13,14] Realizing non-collinear spin polarization in both free and reference layers opens the possibility of achieving sizable tunneling magnetoresistance in Mn_3Sn-based all-antiferromagnetic tunnel junctions (AATJs).[15] Compared with conventional FM-MTJs, NCAF-based junctions offer multiple stable magnetic configurations, showing great potential for future neuromorphic computing applications.

In this paper, we propose AATJ design based on Mn_3Sn free layer and reference layer. We explore the non-collinear spin textures of Mn_3Sn using first-principles calculations, and then analyze the physical mechanism of regulation on non-collinear magnetization in Mn_3Sn by steadily switching the six Néel vector orientations. Besides, we build an all-antiferromagnetic tunnel junction in Mn_3Sn/MgO/Mn_3Sn structure, and the calculated results reveal that the Mn_3Sn-based AATJ can uphold stable TMR from 171% at 50 K

†Corresponding author. E-mail: geyang@tyut.edu.cn

© 2026 Chinese Physical Society and IOP Publishing Ltd. All rights, including for text and data mining, AI training, and similar technologies, are reserved.

to 103% at 350 K in equilibrium. Furthermore, in non-equilibrium state, the TMR of Mn_3Sn-based MTJ can be regulated from 42% to 20% by applied bias from 0.01 V to 0.25 V. Finally, we verified the bias-voltage modulation effect on TMR in Mn_3Sn-based AATJ by transmission coefficient calculations. Our work highlights the feasibility and the potential of Mn_3Sn-based AATJs in antiferromagnetic MRAM, and holds tremendous promise for application in neuromorphic computing by spintronics in the future.

2. Method

First-principles calculations regarding structural optimization, electronic structure analysis, and magnetic characterization are carried out. The projector augmented-wave pseudopotentials and the generalized gradient approximation (GGA) in the Perdew–Burke–Ernzerhof (PBE)[16] form are employed, utilizing the Vienna *Ab initio* Simulation Package (VASP) code.[17,18] The interlayer van der Waals (vdW) interactions are handled by the DFT-D3 method. For these first-principles calculations, a plane-wave energy cutoff of 500 eV and a $13\times13\times1$ Monkhorst–Pack k-point grid are adopted. The structure is optimized through the conjugate gradient method, with the convergence criteria for energy and force set at 1×10^{-5} eV and 0.02 eV/Å, respectively. To avoid the spurious interaction between periodic replicas, a vacuum space with a width of 15 angstroms (Å) is utilized.

The spin-dependent transport calculations are conducted by means of the NANODCAL package.[19] This is achieved through the combination of the nonequilibrium Green's function with DFT.[20] In the spin-dependent transport calculations, the cutoff energy is specified as 80 Hartree, and the basis type employed is double-zeta polarization. For the self-consistent calculations, a $11\times11\times1$ k mesh is utilized. Additionally, the k points used for the calculations of the spin-resolved transmission coefficient and current are also set to be $11\times11\times1$.

At zero bias voltage, the spin-resolved conductance of MTJs can be expressed as

$$G_\sigma = \frac{e^2}{h}\sum_{k_\parallel} T_\sigma\left(k_\parallel, E_\mathrm{F}\right), \tag{1}$$

where $T_\sigma\left(k_\parallel, E_\mathrm{F}\right)$ is the transmission coefficient at the Fermi level (E_F), σ is the spin index ($\sigma=\uparrow,\downarrow$), and the transverse Bloch wave vectors $k_\parallel$. Here e and h are the electron charge and the Planck's constant, respectively.

The spin tunneling current of the MTJ at bias voltage can be obtained using the Landauer–Büttiker[21] formula

$$I_\sigma = \frac{e}{h}\int T_\sigma(E)\left[f_\mathrm{L}(E) - f_\mathrm{R}(E)\right]\mathrm{d}E, \tag{2}$$

where $T_\sigma(E)$ is the spin-resolved transmission spectrum, and $f_\mathrm{L}(E)$ and $f_\mathrm{R}(E)$ are the Fermi–Dirac distribution functions of the left and right electrodes, respectively.

3. Result and discussion

3.1. Spin-resolved electronic structures and noncollinear magnetic switching mechanisms of Mn_3Sn

Firstly, we describe the spin-resolved electronic structures and spin textures in the chiral antiferromagnet material Mn_3Sn (space group $P63/mmc$) obtained by DFT. The primitive unit cell is composed of two atomic layers that are stacked in the direction of the c-axis. In each individual layer, the configuration of three Mn atoms gives rise to a kagome lattice structure, as shown in Fig. 1(a) in pink. Specifically, there is a flat band (FB) along the K–M path near E_F, as indicated by the red arrow in Fig. 1(b). An enlarged view of the band structure in Mn_3Sn is demonstrated in Fig. 1(c). At the same time, the band structure also discloses two pairs of type-II Weyl nodes. Each set comprises two WPs with opposite chirality: W_1^+ and W_1^- are positioned at an energy of approximately $E_\mathrm{F}+50$ meV, and their counterparts W_2^+ and W_2^- are also found at around $E_\mathrm{F}+50$ meV, as marked by the pink arrow along the K–M path in Fig. 1(c). The position of Weyl points controlled by spin texture can be modulated along the assumed node ring (dashed circular curves) via a rotating magnetic field in the xy-plane, as derived without spin–orbit coupling and shown in Fig. 1(d). Such pairs of Weyl nodes with linear dispersion act as sources and sinks of Berry curvature flux.[22] With this distribution of Berry curvature in momentum space, WPs have been proven to be the cause of the polarization direction of the magnetic octupole, which gives rise to the strikingly large anomalous Hall effect (AHE),[23] anomalous Nernst effect (ANE),[24] spin Seebeck effect (SSE), and chiral anomaly[25] in NCAFs.

To further illustrate the distinctiveness of octupole polarization within NCAFs, we depicted the projected density of states (PDOS) that correspond to the positive and negative spin polarizations (Fig. 1(e)), along with the PDOS of magnetic octupoles (Fig. 1(f)). Significantly, in sharp contrast to the symmetric PDOS projected onto the spin-up and spin-down states (Fig. 1(e)), an obvious energy shift was noticed between the majority and minority bands of the octupole moment (Fig. 1(f)). Such imbalance seen in octupole polarization breaks TRS in these antiferromagnetic states, leading to antiferromagnetic TMR effect.

Antiferromagnetic spin textures of Mn_3Sn can be viewed as a ferromagnetic ordering of a cluster magnetic octupole T (Fig. 2(a)), and the corresponding Hamiltonian is illustrated as follows:

$$H = A\sum_{\langle ij\rangle}(m_i\cdot m_j) + D\sum_{\langle ij\rangle} d_{ij}\cdot(m_i\times m_j) - K\sum_i (k_i\cdot m_i)^2. \tag{3}$$

Here, A is the exchange constant,[26] D is the Dzyaloshinskii–Moriya interaction (DMI) strength,[27] and K is the anisotropy constant.[28] The DMI as well as Heisenberg exchange interaction play crucial roles in stabilizing the coplanar non-collinear antiferromagnetic ordering in Mn_3Sn. The single-ion anisotropy term is significantly weaker than both the Heisenberg exchange interaction and DMI terms. This leads to a slight deviation of adjacent Mn magnetic moments from the ideal 120° angle, thereby inducing an extremely small in-plane net moment m with a magnitude of merely a few thousandths of a Bohr magneton per formula unit (mμ_B per f.u.). As depicted by the red arrows in Fig. 2(a), these moments are oriented relative to one another and can undergo coherent rotation within the kagome plane. Therefore, the noncollinear AFM order in Mn_3Sn can be characterized by six Néel vector orientations ($\alpha = 0°$, 60°, 120°, 180°, 240°, 300°), representing the symmetry equivalent AFM states, as shown by the red arrows in Fig. 2(a). It is expected that controlling the orientation of the Néel vector will achieve considerable TMR values, which would enable AATJ. Under the SOT, the sublattice moments and the octupole moment show opposite handedness in Fig. 2(b). The DL effective field acts on the sublattice moments with specific orientations, which facilitates the switching of the non-collinear antiferromagnetic order.

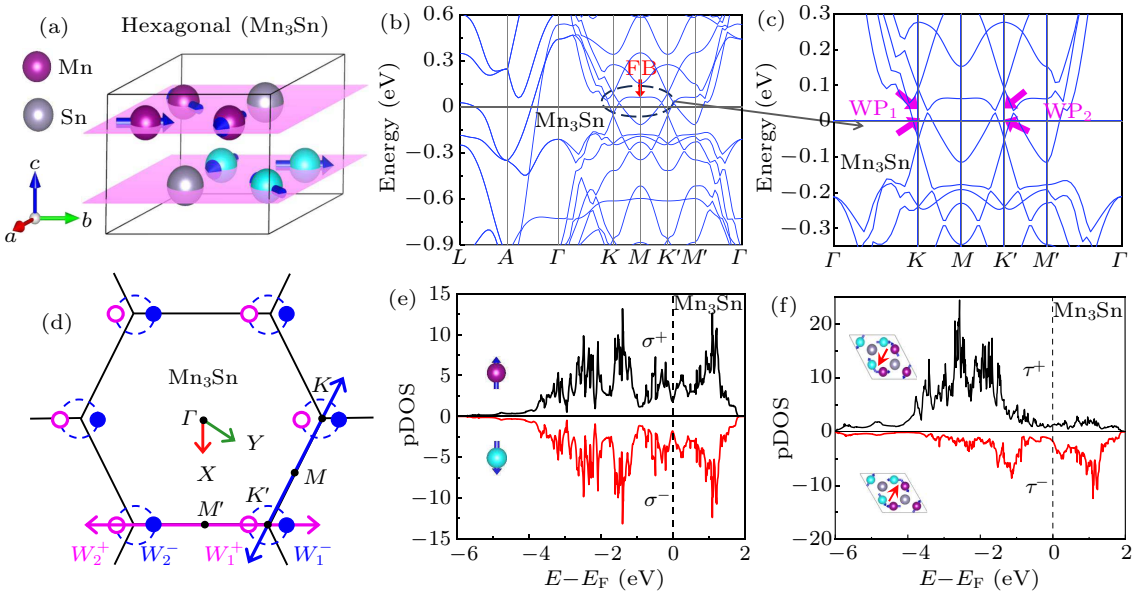


Fig. 1. (a) Crystal structure of Mn_3Sn (kagome planes in pink). (b) Band structure in Mn_3Sn obtained by DFT. FB along K–M' is indicated by the red arrow. (c) An enlarged view of the band structure in Mn_3Sn. WPs along K–M' are indicated by the pink arrow. (d) Weyl points W_1 and W_2 in the $k_z = 0$ plane of the hexagonal Brillouin zone, with open and closed circles indicating positive (+) and negative (−) chirality. (e) Spin-resolved PDOS of Mn 3d orbitals in Mn_3Sn, showing symmetric spin-up and spin-down distributions. (f) Calculated PDOS projected onto octupolar-ordered states for opposite orientations (0° and 180°) in Mn_3Sn. Black and red lines correspond to octupole-majority and minority states, respectively.

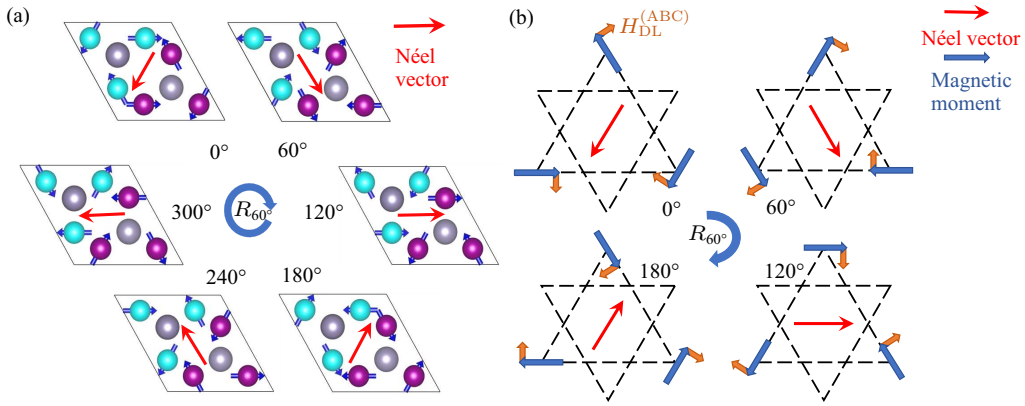


Fig. 2. (a) The top view of atomic and magnetic structures of Mn_3Sn oriented at 0°, 60°, 120°, 180°, 240° and 300°. Blue and purple balls represent Mn atoms in different layers, and blue arrows indicate magnetic moment directions. (b) Schematic of the SOT switching mechanism in non-collinear antiferromagnets. The four subfigures show magnetic states during switching, with the bottom-left panel representing the final stable state. Red arrows denote the Néel vector, blue arrows represent Mn magnetic moments, and orange arrows indicate the direction of the DL effective field.

3.2. TMR and *I*–*V* relation in AATJ

Moving forward, the working principle and advantages of AATJs are further illustrated by comparison with conventional FM-MTJs in terms of state flipping, magnetic disturbance immunity, and integration level, as shown in Fig. 3. In terms of working principles, conventional FM-MTJs have

only two stable magnetic states, thus enabling only binary transmission.[29] In addition, FM-MTJs exhibit a macroscopic magnetic moment, which leads to pronounced magnetic interference between MTJs as the device integration density increases, creating a contradiction between storage density and stability.[30,31] In contrast, NCAFs possess local spin-splitting, ultrafast dynamics (THz), negligible stray field, and ultrafast switching time, enabling simultaneous enhancement of both storage density and storage stability in high-speed AATJs based on NCAFs.[32] Furthermore, they can achieve multivalued switching due to their multiple stable non-collinear magnetization states, applying in the field of brain-inspired computing.

We build Mn_3Sn/MgO/Mn_3Sn AATJ with MgO as the spacer layers to explore the TMR effect. The designed AATJs are divided into semi-infinite left and right Mn_3Sn electrodes and a central region MgO, as shown in the upper left panel of Fig. 3. The heterostructure was constructed using Mn_3Sn (0001) electrodes ($a = 5.59$ Å) and MgO (111) barrier ($a = 5.95$ Å) with biaxial elastic strain (compressive 3.03% on MgO, tensile 3.22% on Mn_3Sn) to achieve a common in-plane lattice constant of 5.77 Å, eliminating the in-plane lattice mismatch. In the computational process, the Néel vector of the left Mn_3Sn electrode is held fixed at $\alpha_L = 0°$, while the Néel vector of the right Mn_3Sn electrode is set to six distinct orientations, specifically $\alpha_R = 0°$, 60°, 120°, 180°, 240°, and 300°. Based on the different Néel vectors of the left and right AFM electrodes, it can achieve multiple nonvolatile states. For $\alpha_R = 0°$, the orientations of the Néel vector have an identical characteristic in the left and right Mn_3Sn electrodes, denoted as the parallel configuration (PC), whereas for $\alpha_R = 180°$, the orientations of the Néel vector are opposite, denoted as the antiparallel configuration (APC) (upper left panel of Fig. 3). It is demonstrated that the tunneling conductance G for PC is 0.4540 (e^2/h) and for APC is 0.1967 (e^2/h). The TMR ratio of Mn_3Sn/insulating barrier/Mn_3Sn MTJ at zero bias voltage is defined as

$$\mathrm{TMR} = \frac{(G_P - G_{AP})}{G_{AP}} \times 100\%. \tag{4}$$

where G_P and G_{AP} represent the total tunneling conductance of the MTJ in the P and AP states, respectively. The conductance ratio is $G_P/G_{AP} \approx 2.31$, and the corresponding TMR ratio is about 131%. This is due to a spin mismatch between the incident electron wave from the left Mn_3Sn electrode and the output electron wave from the right Mn_3Sn electrode.

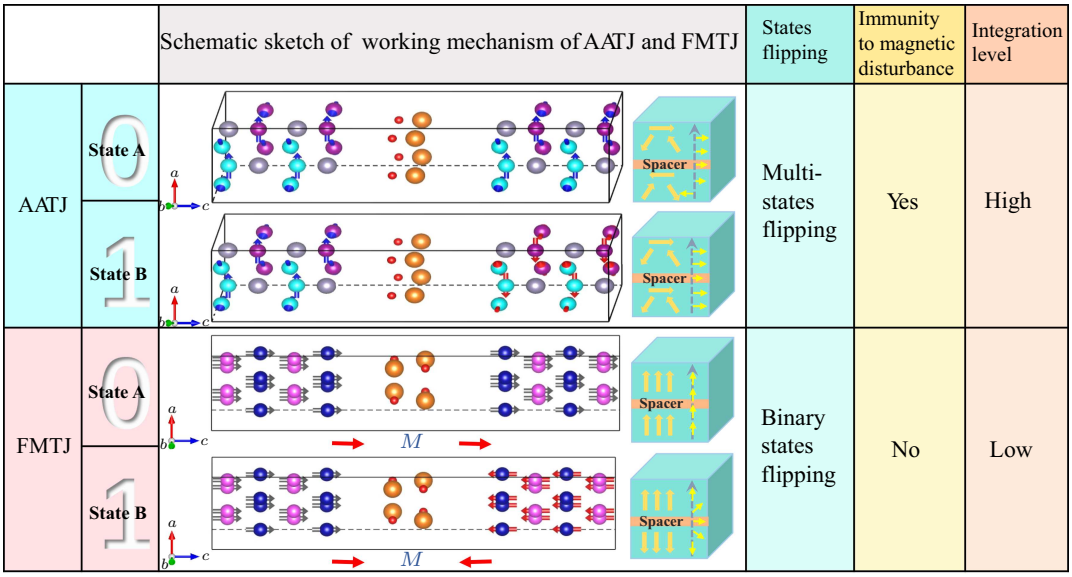


Fig. 3. Comparison of non-collinear antiferromagnet and conventional antiferromagnet. Blue and gray arrows denote the spin polarization of the spin current. The magnetic domains A and B denote two resistance states of low and high resistances in the parallel and anti-parallel states. In the latter case, the collinear ↑↓ spin order induces a fictitious magnetic field even without net magnetization M.

Next, we investigated the transport properties of AATJ in the equilibrium state. To vividly illustrate the impact of voltage bias on the spin-resolved tunnel barriers in the PC and the APC, the PDOS along the transport direction near the E_F is computed by the NEGF method. In Figs. 4(a) and 4(b), the dark blue region around 13 Å corresponds to the MgO barrier. Due to its insulating property, MgO exhibits a low state density over a wide energy range, which efficiently isolates the wave function coupling between the two Mn_3Sn electrodes. A comparison shows that the P state has a much smaller dark blue region and a larger red region than the AP state at the E_F, indicating stronger electronic transport capability in the P state.

Moreover, we analyze the Néel-vector orientation dependence of the zero-bias tunneling conductance and TMR of the Mn_3Sn/MgO/Mn_3Sn AFM MTJ with a fixed Néel-vector orientation of the left electrode (α_L =0°) and different orienta-

tions of the right electrode ($\alpha_R = 0°$, 60°, 120°, 180°, 240° and 300°). As shown in Fig. 4(c), the tunneling conductance can be continuously tuned by the Néel-vector orientation, evolving from the highest value of 0.4540 (e^2/h) in the parallel configuration (PC, $\alpha_R = 0°$) to the lowest value of 0.1967 (e^2/h) in the antiparallel configuration (APC, $\alpha_R = 180°$), followed by a gradual recovery toward the conductance of the parallel state at 360°. Correspondingly, the TMR exhibits a continuous variation as a function of the Néel-vector angle (from 0° to 360°), reaching a maximum value of 131% at the APC. Thus, the TMR ratio can be continuously tuned into multiple states depending on the relative Néel-vector orientation, providing solid evidence for multi-resistance states in noncollinear AFM MTJs, whereas only binary resistance states can be realized in conventional FM MTJs.

In addition, we also calculated the conductance and TMR ratios of the Mn_3Sn/MgO/Mn_3Sn MTJ at varying temperatures. As shown in Fig. 4(d), the TMR exhibits a non-monotonic temperature dependence. It increases from 171% at 50 K to a peak of 192% at 200 K with minor fluctuations. Above 250 K, the TMR drops significantly, reaching 131% at 300 K and 103% at 350 K. The initial rise and stability up to 200 K reflect the robust noncollinear antiferromagnetic order of Mn_3Sn, while the subsequent decline above 250 K is attributed to thermal disruption of magnetic coupling and the MgO barrier properties. These results suggest that the Mn_3Sn/MgO/Mn_3Sn MTJ exhibits stable TMR over a wide temperature range of 50–350 K. The equilibrium transmission spectra versus electron energy for PC and APC show a large transmission contrast in the inset of Fig. 4(d) at 300 K.

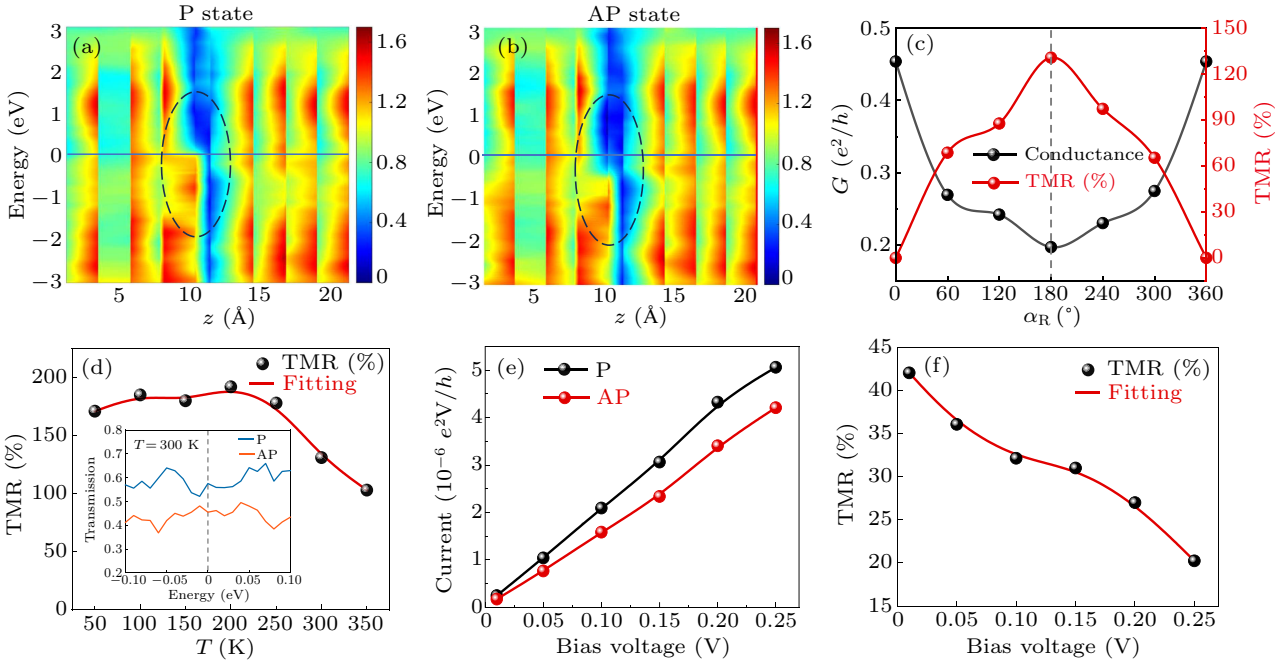


Fig. 4. PDOS along the transport direction (z-axis) for the Mn_3Sn/MgO/Mn_3Sn MTJ in the (a) P state and (b) AP state. (c) Calculated tunneling conductance G (left axis, black curve) and TMR ratio (right axis, red curve) with respect to relative Néel vector rotation angle α_R ranging from 0° to 360°. (d) Temperature-dependent TMR of the Mn_3Sn/MgO/Mn_3Sn MTJ. The inset presents transmission coefficient versus electron energy in PC and APC at equilibrium. (e) Total current and (f) TMR as a function of bias.

Table 1. The calculated I_P, I_{AP} and TMR values with applied bias.

Applied bias voltage (V)	I_P (10^{-6} e^2V/h)	I_{AP} (10^{-6} e^2V/h)	TMR (%)
0.01	0.2462	0.1733	42
0.05	1.0415	0.7654	36
0.1	2.0932	1.5842	32
0.15	3.0629	2.3381	31
0.2	4.3264	3.4068	27
0.25	5.0631	4.2105	20

Then, we explored the bias dependence of the transport properties in the nonequilibrium state in the Mn_3Sn/MgO/Mn_3Sn MTJ. The setup of bias voltage $+v_b$ is described as follows: the left electrode is biased at $+v_b/2$, while the right electrode is biased at $-v_b/2$. The calculated current in the P configuration (I_P), current in the AP configuration (I_{AP}), and corresponding TMR values at different bias voltages are shown in Table 1. It can be seen from Fig. 4(e) that both the I_P and I_{AP} increase monotonically with bias voltage, while the P configuration exhibits a higher current over the entire bias range.

This phenomenon originates from the different transmission capabilities of the two Néel-vector configurations. In the PC, transport with aligned Néel vectors is dominated by high-transmission states near the E_F, with only minor contributions from bias-induced states. In contrast, the APC with reversed Néel vectors exhibits suppressed transmission near E_F, where bias-induced states contribute more significantly to transport.

In this way, the initially suppressed transmission in APC becomes progressively enhanced with increasing bias. Accordingly, both the high-transmission states near E_F in the PC and the bias-induced states in the APC exhibit enhanced electronic transmission, giving rise to increased currents in both configurations. Ultimately, the electron transmission contrast between the two configurations under bias voltage is gradually reduced, leading to a reduction in TMR ratio. As a result, the TMR ratio with applied bias (0.01 V to 0.25 V) in AATJs can be tuned from 42% to 20%, as shown in Fig. 4(f). The TMR ratio under finite bias is calculated by the following definition:

$$\mathrm{TMR} = \left| \frac{I_{\mathrm{PC}} - I_{\mathrm{APC}}}{I_{\mathrm{APC}}} \right| \times 100\%. \tag{5}$$

Furthermore, we verified the bias dependence of the transport properties by relating the transmission spectrum to electron energy in non-equilibrium.[33] A symmetric bias is applied with the left electrode at $+V/2$ and the right electrode at $-V/2$. Transmission spectra versus electron energy for bias voltages ranging from 0.05 V to 0.25 V are presented in Fig. 5. The bias window in each panel is denoted by the yellow shaded regions. As shown in Figs. 5(a) and 5(b), the value of $T_{\mathrm{PC}}(E)$ is higher than that of $T_{\mathrm{APC}}(E)$ at a bias voltage of 0.05 V. According to Eq. (2), the integral of the electron transmission spectrum in the bias voltage window is equal to the current, i.e., the area enclosed by the transmission spectrum and the energy axis in the bias window can approximately reflect the current.[34]

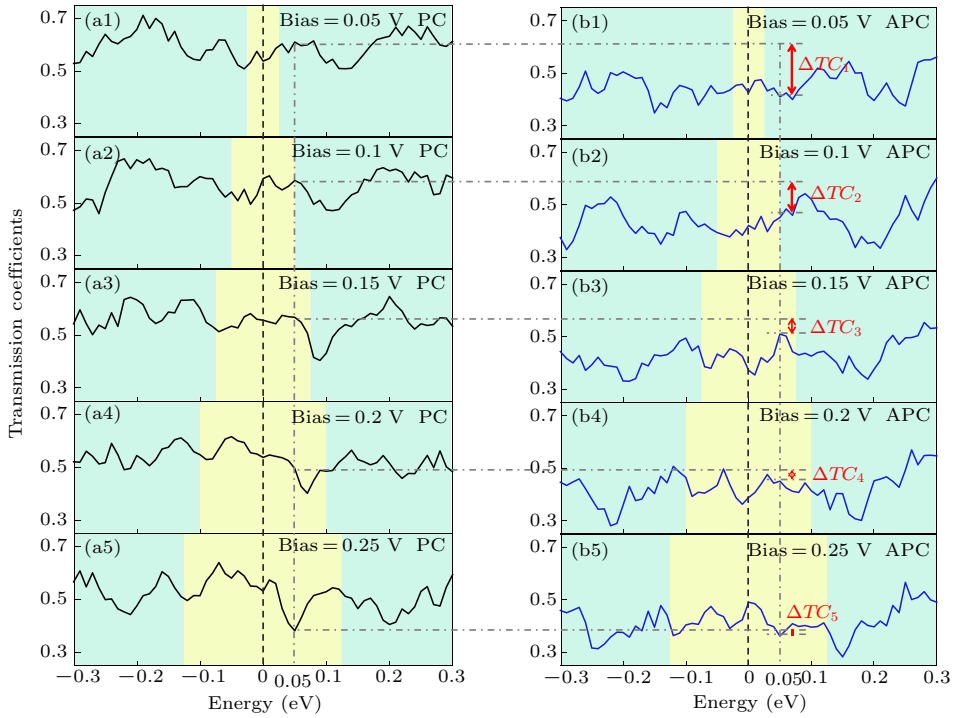


Fig. 5. Total transmission coefficients of the Mn_3Sn/MgO/Mn_3Sn MTJs with (a1)–(a5) P states and (b1)–(b5) AP states as a function of energy at different bias voltages. Black and blue curves represent the transmission coefficients of the P and AP states, respectively. The yellow shadows represent the bias window. The Fermi energy is indicated by the vertical black dashed line. The gray dashed lines mark the transmission coefficients of the PC and APC at E_F+ 50 meV, and the red double-headed arrow highlights the transmission contrast ΔTC between the two configurations.

The applied bias voltage plays a crucial role in the modulation of the electron transmission for the AATJs. At low bias, the bias window falls short of the Weyl-point energy, barely affecting the electron transmission at this moment. As the bias increases, the chemical-potential window sweeps across the chiral Weyl points (around 50 meV above the E_F), which brings about drastic changes in the non-trivial transmission channels driven by Berry curvature. Accordingly, the transmission difference (ΔTC) between the PC and APC around the Weyl-node energy is gradually reduced, as evidenced in Figs. 5(b1)–5(b3), giving rise to the pronounced TMR reduction in Fig. 4(f). Upon further increasing the bias voltage, ΔTC is almost negligible, as shown in Figs. 5(b4) and 5(b5), leading to the convergence of transmission coefficients in PC and APC, resulting in a further suppression of the TMR ratio. This unique bias-dependent tuning ability induced by the Weyl points unveils the microscopic topological origin of TMR modulation in AATJs based on Mn_3Sn fundamentally. In contrast, with the expansion of the transport window, interband tunneling channels induced by bias in conventional FM MTJs reduce the spin-resolved symmetry-selective filtering at the electrode/barrier interface,[35] which is distinguished from the transmission originating from the Weyl points in AATJs based on Mn_3Sn.

4. Conclusion

In summary, chiral antiferromagnetic Mn_3Sn exhibits noncollinear spin textures and octupole polarization arising from broken time-reversal symmetry, providing the physical foundation for the proposed AATJ. Focusing on the noncollinear magnetic switching mechanism, we established the Mn_3Sn/MgO/Mn_3Sn AATJ and clarified its distinct operating mechanism compared with conventional FM MTJs. Furthermore, the tunneling conductance is continuously tunable through the relative orientation of the AFM Néel vectors, demonstrating the feasibility of multi-resistance states in AATJs based on Mn_3Sn. In particular, we explore the TMR effects in AATJs under varying temperatures and bias voltages, while the corresponding transmission spectra of the PC and APC account for the bias-dependent TMR evolution. The novel AATJ is expected to enable ultra-high-density, ultra-high-speed, and low-power antiferromagnetic MRAM, with its multi-valued switching characteristics in spintronics for applications in future brain-inspired devices.

Acknowledgements

This work was supported by the National Natural Science Foundation of China (Grant No. 51975400), Youth Science Foundation of Applied Basic Research Program of Shanxi Province (Grant Nos. 20210302124429 and 202403021222059). We would like to thank the Shanxi Supercomputing Center of China for providing computational resources on TianHe-2 for density functional theory (DFT) calculations by VASP software. We also gratefully acknowledge HZWTECH for generously providing computational facilities to support our transport-related calculations.

References

[1] Shao D and Tsymbal E Y 2024 *NPJ Spintron.* **2** 13
[2] Yang X, Feng W, Zhou X, Mokrousov Y and Yao Y 2024 *Phys. Rev. B* **109** 214406
[3] Scheike T, Sukegawa H, Furubayashi T, Wen Z, Inomata K, Ohkubo T, Hono K and Mitani S 2014 *Appl. Phys. Lett.* **105** 242407
[4] Pertsev N A 2016 *Appl. Phys. Lett.* **109** 132406
[5] Khapikov A F 2001 *J. Appl. Phys.* **89** 7454
[6] Zhou L, Huang J W, Tang M, Qiu C Y, Qin F, Zhang C R, Li Z Y and Wu D 2023 *InfoMat* **5** e12371
[7] Jin W, Li X, Zhang G, Wu H, Wen X, Yang L, Yu J, Xiao B, Guo F, Zhang W, Zhang J and Chang H 2024 *Adv. Funct. Mater.* **34** 2402091
[8] Sim M I, Thian D, Maddu R, Chen X, Tan H K and Li C 2025 *Adv. Funct. Mater.* **35** 2416927
[9] Chen Y, Du Z Z, Lu H and Xie X C 2024 *Phys. Rev. B* **109** L121115
[10] Yu J, Wang X, Guo Y, Fan W and Wang Z 2025 *IEEE Trans. Ind. Informatics* **6** 4789
[11] Levendorf M P, Kim C, Brown L, Huang P Y, Havener R W, Muller D A and Park J 2012 *Nature* **488** 627
[12] Yang Z, Yang X, Wang J, Li Q, Peng R, Lee C H and Ang L K 2025 *Phys. Rev. B* **112** 205202
[13] Vedmedenko E Y, Riego P, Arregi J A and Berger A 2019 *Phys. Rev. Lett.* **122** 257202
[14] Quintes T, Franz M, Thielert P, Redman A J and Richert S 2024 *Chem. Phys. Rev.* **5** 041312
[15] Zhao M, Chen A, Liu E, Zhao L, Wang S, He S, Zhang X and Jiang W 2025 *Chin. Phys. Lett.* **42** 047502
[16] Perdew J P, Burke K and Ernzerhof M 1996 *Phys. Rev. Lett.* **77** 3865
[17] Kresse G and Furthmiiller J 1996 *Comput. Mater. Sci.* **6** 15
[18] Kresse G and Furthmu J 1996 *Phys. Rev. B* **54** 11168
[19] Taylor J, Guo H and Wang J 2001 *Phys. Rev. B* **63** 245407
[20] Randi F and Leifer A M 2021 *Phys. Rev. Lett.* **126** 118102
[21] Jauho A P, Wingreen N S and Meir Y 1994 *Phys. Rev. B* **50** 5528
[22] Li X L, Zhu M, Dong J T, Wu K, Zheng F X and Zhang J 2025 *Chin. Phys. Lett.* **42** 100701
[23] Wang J, Yang X, Yang Z, Lu J, Ho P and Wang W 2026 *Adv. Funct. Mater.* **36** 2505145
[24] Chen T, Tomita T, Minami S, Fu M, Koretsune T, Kitatani M, Muhammad I, Nishio-hamane D, Ishii R, Ishii F, Arita R and Nakatsuji S 2021 *Nat. Commun.* **12** 572
[25] Kang B, Kim M, Park C H and Janotti A 2024 *Phys. Rev. Lett.* **132** 266506
[26] Dong J, Li X, Gurung G, Zhu M, Zhang P and Zheng F 2022 *Phys. Rev. Lett.* **128** 197201
[27] Liu S, Chen T, Wu B, Fan H, Zhu Y, Bi S, Liu Y, Shi Y, Zhang W, Wang M, Li Q, Yang J, Lu J, Zhou T and Liu B 2025 *Adv. Sci.* **12** e02985
[28] Choi Y, Lam H T and Shao S H 2023 *Phys. Rev. Lett.* **130** 131602
[29] Li X, Koo J, Zhu Z, Behnia K and Yan B 2023 *Nat. Commun.* **14** 1642
[30] Chen X, Shi S, Shi G, Fan X, Song C, Zhou X, Bai H, Liao L, Zhou Y, Zhang H, Li A, Chen Y, Han X, Jiang S, Zhu Z, Wu H, Wang X, Xue D and Yang H 2021 *Nat. Mater.* **20** 800
[31] Zhu M, Dong J, Li X, Zheng F, Zhou Y, Wu K and Zhang J 2024 *Chin. Phys. Lett.* **41** 047502
[32] Rizky R, Scheike T, Uzuhashi J, Yasufuku H, Ohkubo T, Wen Z, Mitani S and Sukegawa H 2025 *Mater. Today* **88** 12
[33] Bhattacharya A, Pc S, Ahmed A, Kurebayashi D, Tretiakov O A, Satpati B, Duttagupta S, Alam A and Das I 2025 *Adv. Funct. Mater.* **35** 2424841
[34] Chen H, Nomoto T, Hirschberger M and Arita R 2025 *Phys. Rev. X* **15** 011054
[35] Peralta-Ramos J, Llois A M, Rungger I and Sanvito S 2008 *Phys. Rev. B* **78** 024430